Energy localization in HMX-Estane polymer-bonded explosives during impact loading

A. Barua, Y. Horie, and M. Zhou

Related Articles

Additional information on J. Appl. Phys.

Energy localization in HMX-Estane polymer-bonded explosives during impact loading

A. Barua,[1] Y. Horie,[2] and M. Zhou[1,a)]

[1]*The George W. Woodruff School of Mechanical Engineering, Georgia Institute of Technology, Atlanta, Georgia 30332-0405, USA*

[2]*Air Force Research Lab, Munitions Directorate, 2306 Perimeter Road, Eglin AFB, Florida 32542, USA*

We report the results of a mechanistic study of energy localization in a HMX (High Melting point eXplosive octahydro-1,3,5,7-tetranitro-1,2,3,5-tetrazocine)/Estane PBX system during dynamic loading. The focus is on the thermal-mechanical response over the strain rate range of $10^4 – 10^5$ s^{-1} under different confinement conditions. A recently developed cohesive finite element method is used to track and analyze the contributions to heating from different constituents, interfaces, deformation and fracture mechanisms, and internal friction. In particular, energy dissipations due to viscoelastic deformation, grain fracture, interfacial debonding, and friction along crack faces are quantified as functions of time and overall deformation. The materials analyzed have HMX volume fractions between 0.69 and 0.82. Calculations show that variation in strain rate can significantly affect the spatial distribution but not the overall number of hot spots. Higher confining stresses lead to more intense heating in the binder and more uniform distribution of hot spots. The evolution of hot spots is quantified as a function of loading condition, deformation and microstructural attributes. The microstructure-response relations obtained can be used to assess the initiation sensitivity of energetic composites. © *2012 American Institute of Physics*. [http://dx.doi.org/10.1063/1.3688350]

I. INTRODUCTION

The dynamic response of energetic materials at the grain scale has received significant attention over the past two decades.[1–8] Empirical approaches have been developed[9] to model the response under different loading conditions.[10] Initiation sensitivity is one of the most important considerations for polymer-bonded explosives (PBXs). Shock loading is one type of events that can result in initiation and detonation.[11,12] Initiation and subsequent detonation can also occur under impact loading in the absence of shock.[13] Both types of events require that the mechanisms leading to energy localization need to be better understood.

The initiation of chemical reaction is significantly affected by the local fluctuations of field quantities. The issue partly relates to the formation of hot spots when the materials are subject to mechanical impact. Dissipation associated with mechanisms operative at the grain-level causes localization of thermal energy or the formation of hot spots. Once formed, the hot spots can serve as ignition sites and react exothermally.[14] The hot spots can also lead to deflagration or detonation. In order to predict impact-induced initiation of energetic materials, reactive models can be used.[11,15] For such models to be predictive, account for grain-level phenomena is required. In particular, these models require input such as the distributions of the number, sizes, shapes, and temperatures of hot spots for the particular microstructure and loading involved. For example, in Ref. 15 a hydrodynamic code is used to obtain information regarding the energy localization, growth and micromechanics of hot spots and the information is then used in a reactive model to

resolve the physics at the microscale. Tarver *et al.*[14] analyzed the effects of hot spot geometry and surrounding temperatures on ignition and showed that the critical temperature increases rapidly as the hot spot diameter decreases. Also, the critical times to ignition increases rapidly as hot spot temperatures decrease, indicating that mechanisms producing lower rates of heating must act longer over a sufficiently large volume to cause ignition.

So far, the mechanisms leading to energy localization in PBXs are not well quantified, primarily due to a lack of experimental observations and quantitative analyses at the mesoscale. Because of the inherent heterogeneities in microstructures, several competing failure mechanisms such as deformation of the binder, debonding at the grain-matrix boundary, fracture of grains and frictional contact between crack faces contribute to the dissipation of the energy imparted to the material. Impurities, microcracks and voids can exacerbate the deformation and failure processes and, therefore, significantly affect the ignition sensitivity and hence the performance of the PBX.[16]

While not all dissipation mechanisms directly contribute to heating, they may influence other thermal processes leading to energy localization. For instance, fracture of grains and debonding at grain-matrix boundary result in the creation of new surfaces. Localized frictional dissipation occurring along these fractured surfaces, however, can lead to very high temperatures which in turn can cause melting of the granules and subsequent reaction initiation.

Clearly, the mechanisms responsible for energy localization are complex and a systematic study is needed to evaluate their contributions to the ignition sensitivity of a PBX. The stochastic nature of microstructural heterogeneities such as varying grain size and random constituent morphologies

a)Electronic mail: min.zhou@me.gatech.edu.

necessitate a statistical approach in the quantification of hot spot formation. In addition, loading conditions (such as strain rate and degree of confinement) influence the rate and manner in which mechanical work is imparted to the material, thereby affecting the localization of energy. Realistic characterization must consider these factors.

Quantification of the contributions of different dissipation mechanisms and how the contributions evolve as deformation progresses is essential in order to develop predictive models that can be used to characterize the formation of hot spots. In the analysis reported here, a recently developed Lagrangian cohesive finite element framework is used to quantify the effects of microstructure and thermal-mechanical processes such as matrix deformation, interfacial debonding and fracture of grains on hot spot formation. Simulations are carried out for a range of strain rates, grain volume fraction and confinement condition. The focus is characterizing energy localization as a function of loading and microstructural attributes. The ultimate objective is to understand and quantify the mechanisms leading to initiation in energetic materials. The analysis will help create microstructure-performance maps for the development of PBXs with tailored attributes. The details of the theoretical framework used are published in Ref. 17 so only a brief overview is provided here.

II. MICROSTRUCTURE MODELING

This analysis focuses on two-phase microstructures consisting of HMX grains in an Estane binder [see Fig. 1(a)]. Both idealized and actual microstructures are used. The actual microstructure is obtained from Ref. 10 and its grain volume fraction is digitally varied between 0.69 and 0.82. The micrographs are given and quantified in Ref. 17. Additionally, a set of six idealized microstructures are used. These are generated using 2D Voronoi tessellation functions in MATLAB. This approach allows multifaceted grains with morphologies similar to those of actual HMX grains to be obtained. Previously, Wu *et al.*[18] used a similar approach to generate idealized PBX microstructures. Figure 1(a) shows a representative idealized microstructure having a grain volume fraction of $\eta = 0.69$. The grain size distributions for this set of six microstructures are similar and have means between 203.6 and 224.2 μm and standard deviations between 86.6 and 111.4 μm [e.g. the grain size distribution for the microstructure in Fig. 1(a) is shown in Fig. 1(b)]. The microstructures analyzed, along with their attributes are listed in Table I. Together, these allow us to evaluate the statistical variation in response for microstructures having similar attributes.

The calculations are performed on a 3-mm square microstructural region. This sample size is at least one order of magnitude larger than the length scale of the mean grain size for this type of PBX, giving reasonable representation of the microstructures. The specimen is initially stress-free and at rest. The loading configuration shown in Fig. 2 is designed to account for a range of loading rates and different load triaxiality levels. The velocity boundary condition at the top surface and the fixed displacement boundary condition at the bottom surface allow prescribed overall deformation rates to
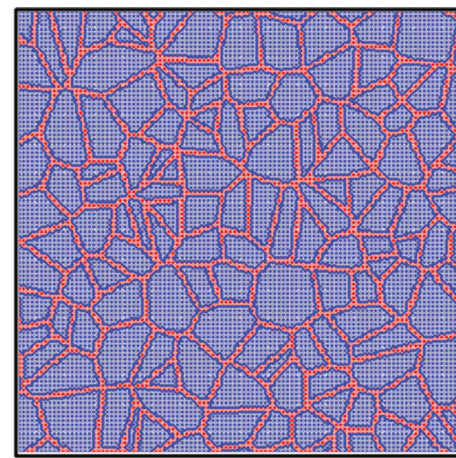
(a) Microstructure – 1
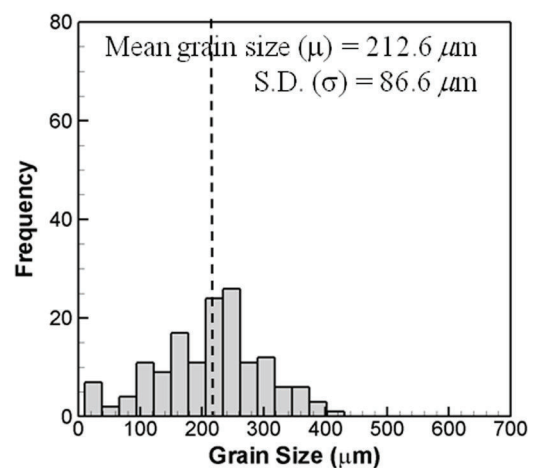
(b) Grain Size Distribution

FIG. 1. (Color online) (a) A representative idealized microstructure with a grain volume fraction of $\eta = 0.69$ and (b) the grain size distribution of the microstructure.

be imposed. The strain-rate $\dot{\varepsilon}$ is calculated by dividing the velocity of the top surface v by the initial height of the specimen. The lateral sides have imposed velocity v_L, where $0 < v_L < v$, allowing the degree of confinement to be varied from nominally uniaxial strain to nominally uniaxial stress. In the calculations carried out here, three confinement levels are considered, (1) uniaxial strain ($v_L = 0$), (2) $v_L/v = 0.5$, and (3) uniaxial stress (v_L not specified, lateral sides are traction-free). This is a 2D model and the conditions of plane-strain prevail.

The finite element framework uses linear triangular bulk elements which are interspaced by 4-noded cohesive elements, distributed throughout the mesh at all bulk element interfaces. The cohesive elements follow a traction-separation law relating the traction on the cohesive surface pair to the interfacial separation. The bilinear traction-separation law developed by Zhai and Zhou[19] is used in case of tensile and shear separations. Under compression, a penalty traction is used to strongly discourage interpenetration of cohesive surfaces. Failure of cohesive elements results in creation of new surfaces. In order to prevent interpenetration

TABLE I. Microstructures analyzed.

Microstructure	Grain volume fraction (η)	Average grain size (μm)	Standard deviation (μm)	N_A (mm^{-2})
Digitized	0.69	214.0	108.9	12.08
Digitized	0.77	238.0	121.4	14.17
Digitized	0.82	287.4	120.6	11.10
Idealized (6 instantiations)	0.69	203.6 – 222.4	86.6 – 111.4	–

of failed surfaces, a contact algorithm is used to apply a normal penalty force to prevent the overlap of elements. The Coulomb friction law is used to determine the frictional force between contacting surface pairs.

The binder is modeled using a finite deformation viscoelastic model. A 22-element Prony series from Ref. 20 is used to characterize the variation of the shear modulus with the relaxation time. For the HMX granules, a hyperelastic constitutive model is used. The cohesive elements are embedded throughout the entire finite element mesh, at all bulk element interfaces. This allows arbitrary crack/microcrack patterns to be resolved. Specifically, fracture of the grains, debonding at the grain/matrix interfaces, and tearing of the binder can be tracked explicitly. This study focuses on non-shock conditions, therefore, the HMX grains undergo very little plastic deformation, justifying the use of a hyperelastic model for the HMX grains. The constitutive parameters for HMX, Estane, and the cohesive interface properties are given in Ref. 17.

III. RESULTS AND DISCUSSIONS

A parametric study is carried out, focusing on the effects of (i) strain rate, (ii) confinement, and (iii) grain volume fraction ($\eta = 0.69$ to 0.82). For all calculations presented, the initial temperature is $T_i = 300$ K. The velocity v_0 of the top surface is varied between 50 to 300 ms^{-1}, yielding overall strain rates of $\dot{\varepsilon} = (16.6 - 100) \times 10^3$ s^{-1}. The velocity is imposed at the top surface of the configurations in Fig. 2, with a linear ramp from zero to v_0 in the first 2 μs of loading. Unless otherwise noted, the nominal strain rate used is $\dot{\varepsilon} = 16.6 \times 10^3$ s^{-1}.

The overage velocity of the stress waves in the microstructure varies with the binder volume fraction of the PBX. For $\eta = 0.82$, the wave velocity is 2.65×10^3 ms^{-1}. The wave reaches the bottom surface at 1.1 μs. Since the top boundary is displaced at a constant velocity, the stress state in the sample can be considered as nominally homogeneous after the stress wave reaches the bottom surface. Analysis yields similar results for the other volume fractions considered.

A. Methodology for detection of hot spots

To determine the size and temperature distributions of hot spots, a systematic scheme is used. A "microscope" with an inner diameter d_i and outer diameter d_o sweeps through the microstructure to identify potential hot spots (see Fig. 3). The process involves the use of a threshold temperature (ΔT_{thres}). At each time step, the microstructure is scanned by calculating the average temperature over successive circular regions of diameter d_i. If the average temperature in the region exceeds the average temperature in the annulus region defined by d_i and d_o surrounding it by ΔT_{thres}, the region is identified as a hot spot.

The choice of the threshold temperature ΔT_{thres} and sieve diameters d_i, and d_o are somewhat arbitrary. To identify the trend, different values for d_i, d_o and ΔT_{thres} are used. First, d_i and d_o are held constant while ΔT_{thres} is varied. Figure 4(a) shows the variation of the number of hot spots with ΔT_{thres} at the nominal strains of $\varepsilon = 6.0$ and 8.6%. As ΔT_{thres} increases, the number of hot spots initially decreases but gradually attains a steady value beyond $\Delta T_{\text{thres}} = 20$ K. This value of ΔT_{thres} is used for all subsequent hot spot analyses.

Similarly, in order to select the appropriate critical size value, d_i ($d_o = 2d_i$) is varied with $\Delta T_{\text{thres}} = 20$ K. The results in Fig. 4(b) show that higher critical diameter values yield lower numbers of hot spots, however, beyond a critical diameter of $d_i = 0.06$ mm, the number of hot spots remain essentially the same. This trend is consistent at all strain values.
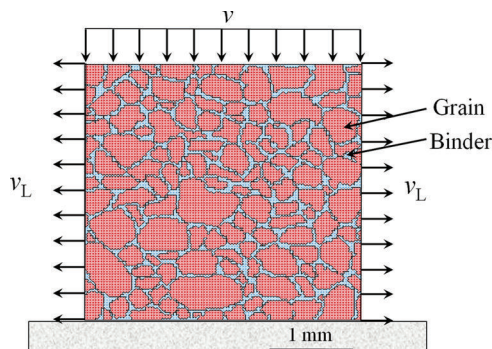

FIG. 2. (Color online) Loading configuration with impact velocity v on the top surface and with the lateral sides having fixed or traction-free boundary conditions which correspond to confined or unconfined specimens, respectively.
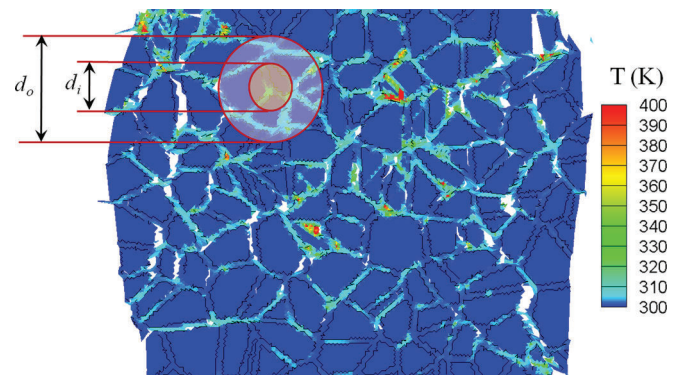

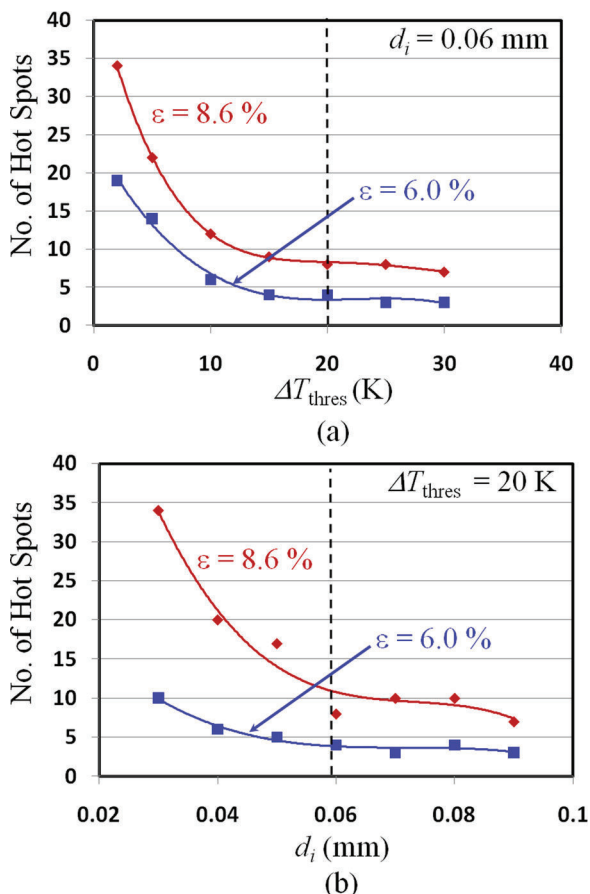FIG. 3. (Color online) Scheme for hot spot detection.

FIG. 4. (Color online) (a) Number of hot spots detected using different threshold temperatures; (b) number of hot spots detected using different critical sizes ($\eta = 0.69$, $\dot{\varepsilon} = 16.6 \times 10^3 \, \text{s}^{-1}$).

The distribution of hot spots in the microstructure with $\eta = 0.69$ at a strain rate of $16.6 \times 10^3 \, \text{s}^{-1}$ and strain of $\varepsilon = 0.06$ is shown in Fig. 5. The locations of the hot spots detected using different values of d_i overlap, suggesting that the approach used to define and identify hot spots produces results consistently. Although the specific threshold for defining hot spots is somewhat arbitrary, the approach has a benefit in that it allows the size distributions of hot spots in different cases to be compared on a relative basis. Note that most hot spots occur at locations of grain-grain interactions and are captured when the sieve size is in the range of $d_i = 0.06{-}0.12 \, \text{mm}$. This size range corresponds to the aver-
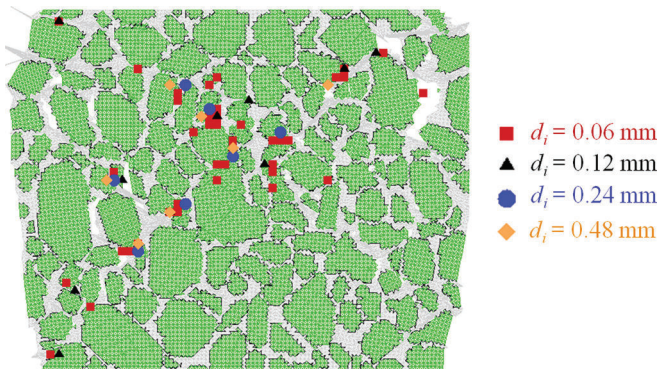
age thickness of the binder for microstructures with $\eta = 0.69$. At higher values of d_i, fewer hot spots are detected and are more sparsely distributed spatially. In all subsequent calculations, a critical size of $d_i = 0.06 \, \text{mm}$ is used. The evolution of hot spots is dependent on several time-dependent thermo-mechanical processes. We first present one set of calculations to illustrate the mechanisms responsible for hot spot formation.

B. Variation in response among microstructures with the same statistical attributes

A set of six idealized microstructures is used in the analysis. These microstructures are different instantiations with the same statistical attributes [$\eta = 0.69$, grain size distribution in Fig. 1(b)]. The overall strain rate is $16.6 \times 10^3 \, \text{s}^{-1}$. Figure 6(a) shows the distribution of temperature at $\varepsilon = 0.05$ for microstructure 1 [shown in Fig. 1(a)]. Initially, temperature rises due to viscoelastic dissipation in the soft binder. As the binder deforms, damage occurs through grain-matrix debonding and tearing of the binder. These mechanisms allow neighboring grains to come into contact with each other, causing subsequent fracture and frictional dissipation. At higher levels of overall deformation, transgranular fracture occurs. Figure 6(b) shows the distribution of hot spots at $\varepsilon = 0.05$. A majority of the hot spots occur at locations of grain–grain interactions. These locations are characterized
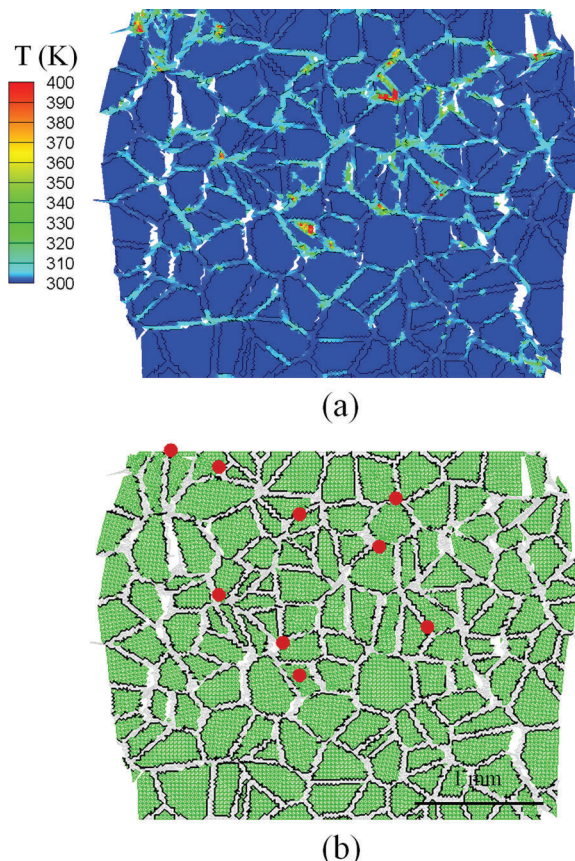

(a)

(b)

FIG. 6. (Color online) (a) Distribution of temperature in the idealized microstructure in Fig. 1(a) and (b) distribution of hot spots ($t = 4.2 \, \mu\text{s}$, $\varepsilon = 0.05$ and $\dot{\varepsilon} = 16.6 \times 10^3 \, \text{s}^{-1}$).

FIG. 5. (Color online) Hot spot detected using different values of d_i.

by severe stress concentration, crack development and grain-matrix sliding.[17]

The failure processes are highly nonlinear and the response of the material is consequently stochastic. Here, the statistical variations in the stress-strain relation and the hot spot count due to microstructural sample differences are characterized. Figure 7 shows the stress-strain relations at a strain rate of $\dot{\varepsilon} = 16,667$ s^{-1} for the six idealized microstructures with $\eta = 0.69$. In the early stages of loading, deformation is primarily accommodated by the softer binder. Consequently, the variation in the stress-strain responses between the samples is small. Specifically, the variation is ~6% up to a nominal strain of 0.04. As the nominal strain increases to 0.11, the variation in the stress-strain curves increases to 16%. The stress level at larger strains is influenced by two competing failure mechanisms: softening resulting from debonding at the grain–matrix interfaces and stiffening due to grain–grain interactions.

Figure 8 shows the evolution of the number of hot spots with the nominal strain for the six idealized microstructures. Unlike the variation in the stress-strain curves, the evolution of the number of hot spots is more consistent among the specimens.

The evolution of hot spots is directly related to the dissipation of energy. Figure 9 shows the evolution of various forms of work and energies per unit volume of the specimen. The total mechanical work imparted to the microstructure by the applied load or boundary work (W_b) increases nearly linearly to 8 MJ/m^3 as the nominal strain reaches 0.08. Initially, a larger portion of W_b is converted to kinetic energy (W_k) and viscoelastic dissipation (W_{ve}) in the binder dominates. Beyond a nominal strain of 0.04, intergranular interactions cause frictional dissipation (W_f) to occur. Up to this strain, viscoelastic dissipation is the dominant contributor to temperature rise. The rate of increase of W_f is typically higher than that of W_{ve}. The difference eventually causes a transition in heating mechanism, as reported in Ref. 21. The higher heating rate eventually leads to the formation of hot spots. The coincidence between the strain (~4%) for the onset of hot spot formation (Fig. 8) and the time for the onset

FIG. 8. (Color online) Evolution of hot spots with nominal strain for six idealized microstructures with the same statistical attributes ($\eta = 0.69$, $\dot{\varepsilon} = 16.6 \times 10^3$ s^{-1}).

of frictional dissipation (Fig. 9) show that the formation of hot spots is closely related to the initiation of frictional dissipation. This will be further discussed later in the paper.

C. Distribution of hot spots

The formation of hot spots is analyzed over a range of strain rates and confinement conditions for PBXs with different volume fractions. A number of studies have focused on the effect of strain rate and the effect of constituent binders.[2,3,22,23] It is generally acknowledged that the rate dependency of the polymeric binder significantly influences the response of the composite. Corley et al.[24] used a nonlinear viscoelastic material model to predict the high strain rate behavior of a particulate composite with hydroxyl-terminated polybutadiene (HTPB) as the binder. Rate dependency also influences microstructure-specific damage evolution which is difficult to quantify using analytical models.

The effect of strain rate is analyzed by deforming the microstructure in Fig. 2(a) of Ref. 17, henceforth referred to
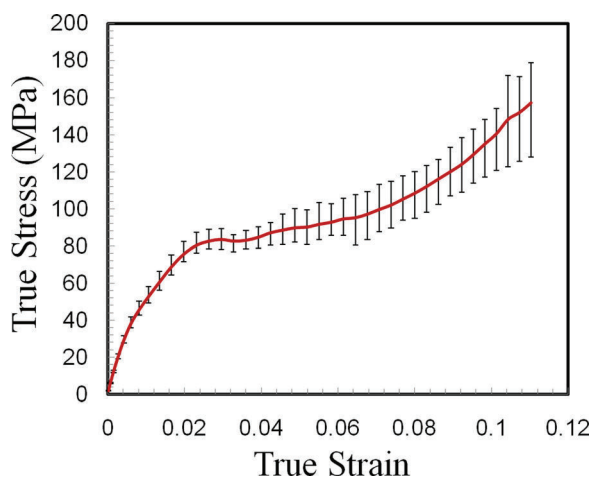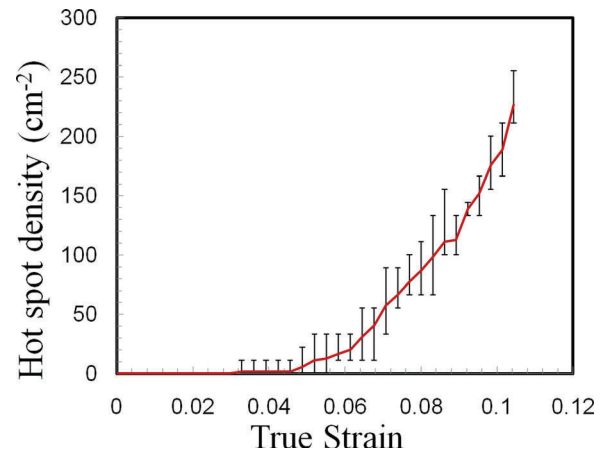

FIG. 7. (Color online) Stress-strain relations for six idealized microstructures with the same statistical attributes ($\eta = 0.69$, $\dot{\varepsilon} = 16,667$ s^{-1}).
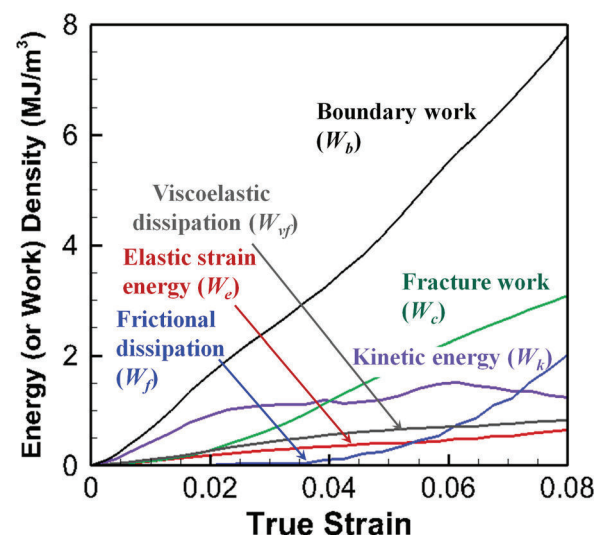

FIG. 9. (Color online) Evolution of mechanical work and energy dissipations for idealized microstructure −1 shown in Fig. 1 ($\eta = 0.69$, $\dot{\varepsilon} = 16.6 \times 10^3$ s^{-1}).

as microstructure A, at four strain rates in the range of $\dot{\varepsilon} = (16.6 - 100) \times 10^3$ s^{-1}. Figure 10 shows the distributions of temperature at a nominal strain of 0.05. At lower strain rates, the binder is softer and more prone to shear banding. This allows viscoelastic deformation to be spread out over the entire microstructure. Significant debonding of the grain–matrix interface occurs at the lower rates. Viscoelastic dissipation in the binder causes temperature to increase along the shear bands. These bands tend to follow the directions of the principle shear stresses in the specimen. In contrast, at higher strain rates the binder is much harder and resists deformation to a greater extent, resulting in less shear banding and concentration of deformation near the impact surface. Higher overall stresses are also generated in the grains and cause fracture in grains to occur earlier. At higher strain rates, there is intense heating near the impact surface. The heating in the binder is also accompanied by frictional dissipation at fractured surfaces.

Figures 11(a) and 11(b) show the distribution of hot spots for the strain rates of 16.6×10^3 and 10^5 s^{-1} at a nominal strain of 0.1. Two different mechanisms take prominence at the two rates. At the lower strain rate, shear banding in the binder (along with debonding) is the primary mode of failure. This allows grains to come into contact with each other along the shear band. These locations are sites of severe stress concentration, crack development and grain-matrix sliding. As a result, the hot spots are distributed preferentially along the shear bands [see Fig. 11(a)]. At the higher strain rate [see Fig. 11(b)], the distribution of hot spots is concentrated near the impact face where the most severe temperature rises occur. The hot spots are not uniformly distributed and seem to occur in clusters. The hot spots occur both inside grains and between grains, in contrast to what is seen in Fig. 11(a) where all hot spots are located in between grains. The formation of hot spots inside the grains is a result of grain fracture and subsequent frictional dissipation along the fractured surfaces.

The evolution of the number of hot spots as a function of strain for the four strain rates between $\dot{\varepsilon} = 16.6 \times 10^3$ and 10^5 s^{-1} is summarized in Fig. 12(a). The overall numbers of hot spots are similar at the different strain rates. This trend is seen for other microstructures with different volume fractions as well (results not shown).

In applications, it is desirable to have higher grain volume fractions for larger energy output. However, this decreases the amount of binder available for absorption of the impact energy. Figure 11(c) shows the distribution of hot spots for $\eta = 0.82$ at a strain rate of 16.6×10^3 s^{-1}. Clearly, the number of hot spots is higher compared with the case for $\eta = 0.69$ [Fig. 11(a)]. Additionally, for $\eta = 0.82$, a larger number of hot spots occur inside the granules as a result of more extensive transgranular fracture, in contrast to what is seen in Fig. 11(a) for $\eta = 0.69$. It is interesting to note that for both levels of η, the hot spots are distributed preferentially along the shear bands, signifying that the effect of shear banding is not significantly affected by the volume fraction.

Volume fraction also significantly affects the evolution of hot spots. In Ref. 17 it was shown that increasing the volume fraction resulted in earlier frictional heating and higher temperatures. Figure 12(b) shows evolution of the hot spot density (per unit area) with nominal strain for $\eta = 0.69 - 0.82$ at $\dot{\varepsilon} = 16.6 \times 10^3$ s^{-1}. Clearly, the hot spot density increases with η, for the same value of overall strain.

(a) $\dot{\varepsilon} = 16.7 \times 10^3$ s^{-1}

(b) $\dot{\varepsilon} = 33.3 \times 10^3$ s^{-1}

(c) $\dot{\varepsilon} = 66.7 \times 10^3$ s^{-1}
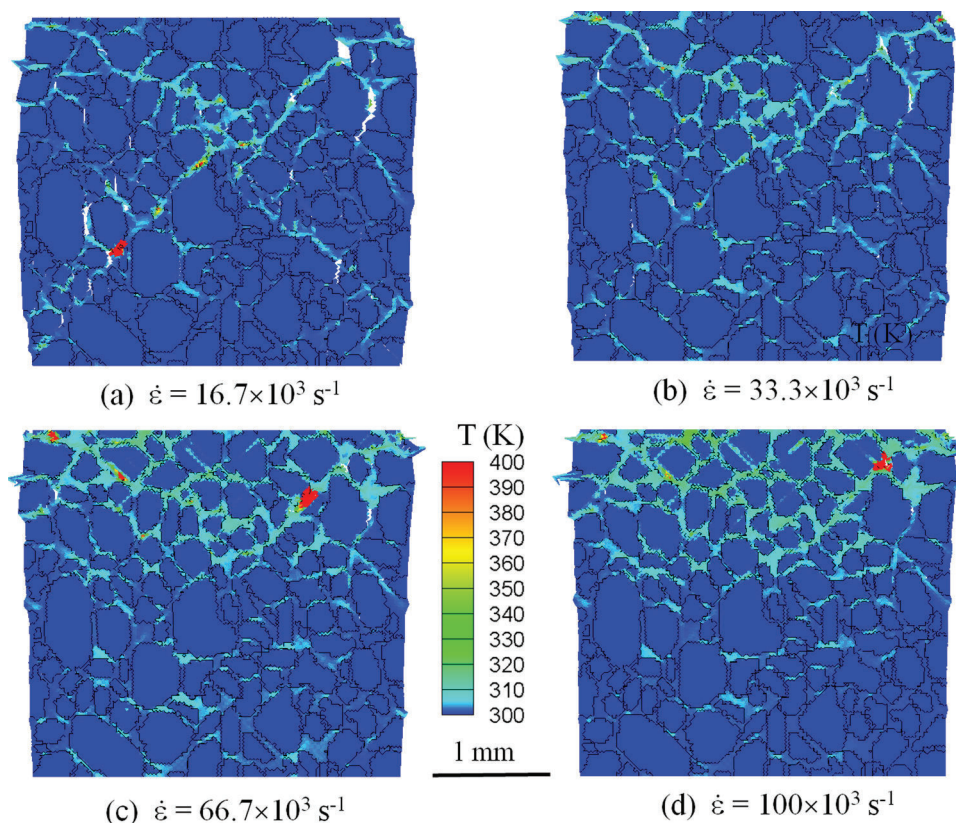
(d) $\dot{\varepsilon} = 100 \times 10^3$ s^{-1}

FIG. 10. (Color online) Distribution of temperature for the strain rates of (a) 16.6×10^3 s^{-1}, (b) 30×10^3 s^{-1}, (c) 66.7×10^3 s^{-1}, and (d) 10^5 s^{-1} at $\varepsilon = 5.0\%$ ($\eta = 0.69$).
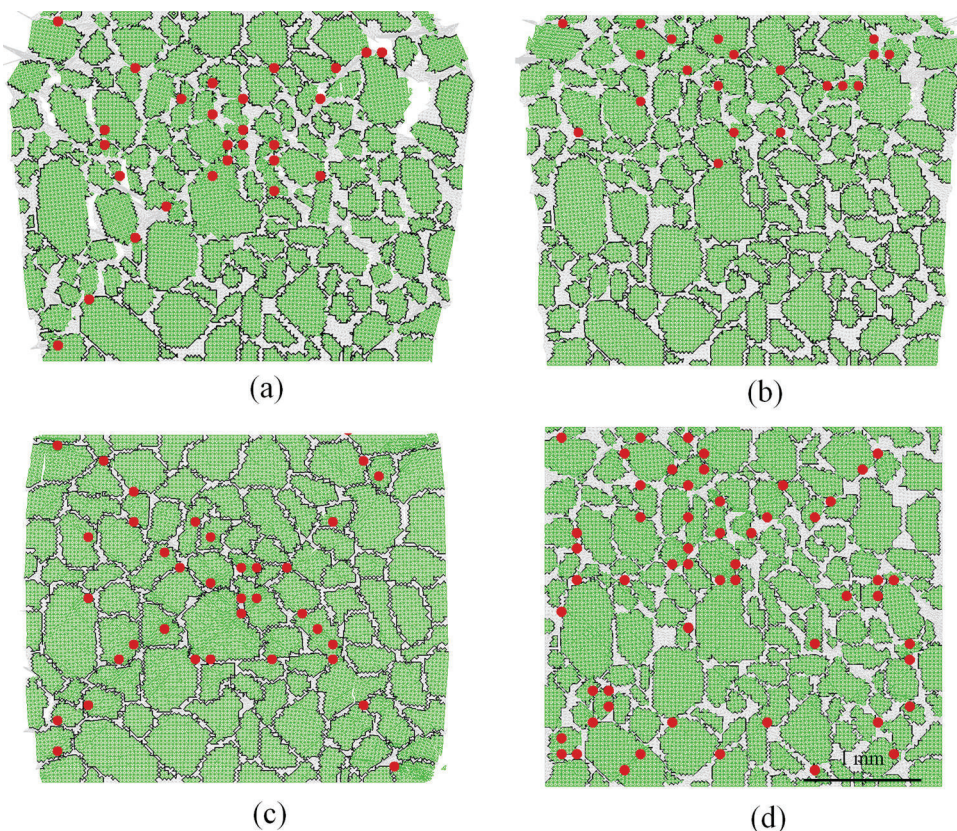
FIG. 11. (Color online) Distribution of hot spots at $\varepsilon = 9.0\%$, for an unconfined specimen with (a) $\eta = 0.69$ at $\dot{\varepsilon} = 16.6 \times 10^3$ s^{-1}, (b) $\eta = 0.69$ at $\dot{\varepsilon} = 10^5$ s^{-1} (c) $\eta = 0.82$ at $\dot{\varepsilon} = 16.6 \times 10^3$ s^{-1}, and (d) confined specimen with $\eta = 0.69$ at $\dot{\varepsilon} = 16.6 \times 10^3$ s^{-1}.

Higher packing densities decrease the inter-particle distance, thereby enhancing grain-grain interactions and intensifying heating. Additionally, denser packing results in higher stress levels in the grains and the microstructures in general. Both mechanisms tend to increase the rate of hot spot forma-tion. This effect is qualitatively similar to that of increasing confinement.

The response of a PBX is also strongly influenced by the confinement conditions. Wiegand et al.[25] studied the mechanical properties of explosives as a function of mechanical

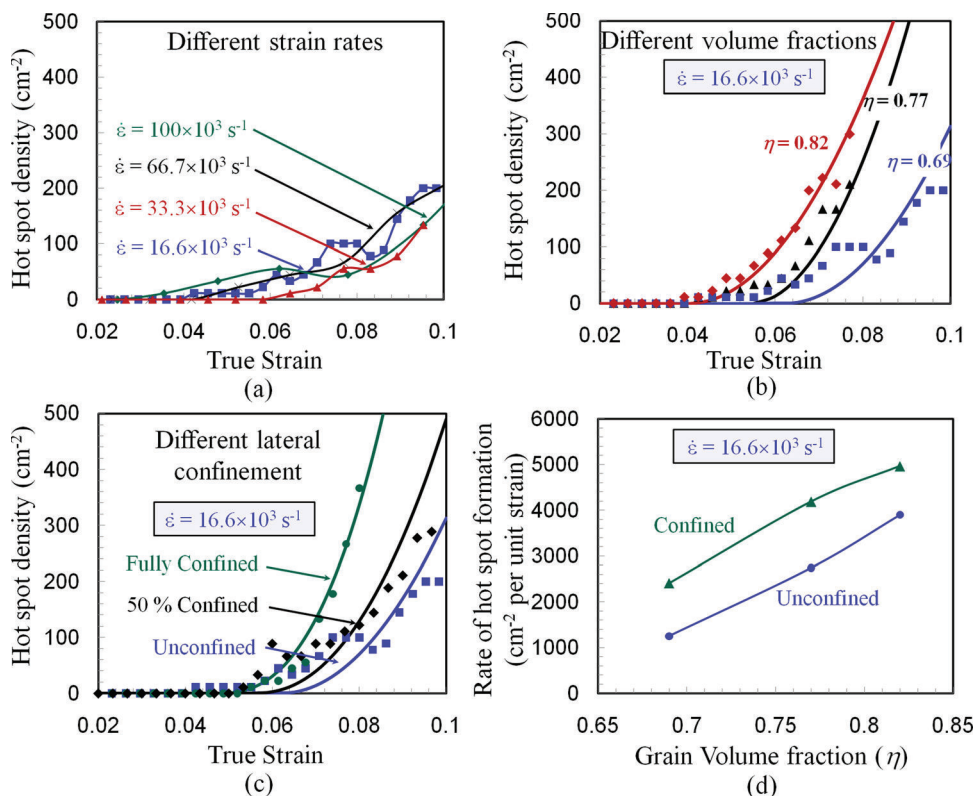FIG. 12. (Color online) Evolution of hot spots for (a) different strain rates ($\eta = 0.69$), (b) different volume fractions ($\dot{\varepsilon} = 16.6 \times 10^3$ s^{-1}, unconfined), (c) different lateral confinement ($\dot{\varepsilon} = 16.6 \times 10^3$ s^{-1}, $\eta = 0.69$), and (d) average rate of hot spot formation (averaged up to $\varepsilon = 0.73$, $\dot{\varepsilon} = 16.6 \times 10^3$ s^{-1}).

confinement at low strain rates. The authors reported that there is a significant increase in modulus and flow stress as the confinement stress increases. In the case of unconfined samples, the dominant failure mechanism is crack propagation; while for samples under confinement, the dominant failure mode is plastic deformation. Here, we discuss calculations using microstructure A, at a strain rate of $\dot{\varepsilon} = 16.6 \times 10^3 \ \mathrm{s}^{-1}$.

Figure 11(d) shows the distribution of hot spots at an overall strain of 9.0% for the confined case. The high level of stress triaxiality enhances frictional heating and causes the hot spots to be more evenly distributed spatially compared with the unconfined case in Fig. 11(c). As seen previously, a high proportion of the hot spots are generated at locations of grain–grain interactions. Figure 12(c) shows the evolution of the density (number per unit volume) of hot spots with nominal strain for the different cases of confinement. For $\varepsilon < 5.0\%$, the unconfined case has more hot spots due to more extensive debonding at the grain–matrix interfaces and the intense shear deformation of the binder matrix. At $\varepsilon > 5.0\%$, the higher stress triaxiality in the confined cause causes a larger number of hot spots to form, owing to the fact that fracture occurs primarily through shear failure and higher compressive stresses on crack faces give rise to more intense frictional heating in later stages of deformation.

D. Quantification of the evolution of hot spots

It is desirable to quantify the formation of hot spots as a function of loading conditions and microstructural attributes. The results can be used to obtain useful insight into the relative importance of energy localization mechanisms under different loading scenarios and microstructural settings.

We first determine the microstructural attributes which may influence the distribution of hot spots. The most obvious one is the volume fraction η. Under the same conditions, a higher volume fraction leads to a higher number of hot spots. However, η is a measure of the overall grain fraction and does not give any information regarding the size or distribution of grains. The failure mechanisms leading to energy localization occur at the grain level. Consequently, the distribution of hot spots is also influenced by the grain size and morphology. It is difficult to obtain a direct correlation between the size distribution and the number of hot spots since a single grain can interact with multiple neighboring grains.

One way to assess the combined effect of size and shape of grains is to estimate the number of potential locations of grain–grain interactions. This can be estimated by analyzing the 2D micrographs using a set of parallel test lines and counting the number of phase boundaries encountered by the test lines. Let P_L represent the number of phase boundaries encountered per unit length and $\bar{P}_L$ be the average value of P_L measured over the entire specimen. It is assumed that the grains are convex in shape (i.e., a test line intersects any grain at only two locations). In such a situation, $(1/2)\bar{P}_L$ represents the average number of grain–grain interactions per unit length. It can be further shown that for any given two phase microstructure,[26]

$$\bar{P}_L = \frac{S_V}{2},\tag{1}$$

where, S_v is the total area of grain-matrix interfaces per unit volume. For an isotropic microstructure, P_L can be assumed to be identical for test lines in any orientation. Thus, N_A, which is proportional to the number of potential sites for hot spot formation, per unit area (2D) is

$$N_A = \left(\frac{\bar{P}_L}{2}\right)^2 = \left(\frac{S_V}{4}\right)^2\tag{2}$$

and the number per unit volume is

$$N_V = \left(\frac{\bar{P}_L}{2}\right)^3 = \left(\frac{S_V}{4}\right)^3.\tag{3}$$

The parameter N_v (or N_A), incorporates the effects of both grain size and distribution and is applicable for all two phase microstructures having convex shaped grains. We note that the effect of grain morphology is not explicitly considered by N_v (or N_A). The effect of morphology may be the subject of a future study. The values of N_A for the microstructures analyzed, are listed in Table I.

The rate at which hot spots are formed is a function of nominal strain. For all calculations, hot spots do not develop until a delay time (t_d) or delay strain (ε_d) has elapsed. The delay strain is the nominal strain at which the dominant heating mechanism changes from viscoelastic dissipation in the binder to frictional heating at fractured surfaces where frictional dissipation occurs.[21] This strain primarily dependents on the packing density of the composite. Once hot spots start to form, the evolution of the number count can be described by a power-law function of the nominal strain.

In general, the evolution of hot spots with strain can thus be expressed as a function in the form of

$$H = H\{\eta, N, \alpha, \varepsilon, \dot{\varepsilon}\},\tag{4}$$

where H represents the number of hot spots per unit volume at any given level of nominal strain ε, N ($= N_V$ in 3D or N_A in 2D) measures the number of potential hot spot sites per volume and α is a parameter which measures the rate of growth of the hot spot density.

Calculated results show that, for the conditions analyzed confinement significantly influences the hot spot count. In contrast, H is quite insensitive to strain rate, although the spatial distribution of hot spots are different at different strain rates [see Figs. 11(a) and 11(b)].

The form that provides a good description of the hot spot data is

$$H(\varepsilon) = \begin{cases} 0, & 0 \leq \varepsilon \leq \varepsilon_d; \\ K\eta N\left(\frac{\varepsilon}{\varepsilon_d(\eta)} - 1\right)^\alpha, & \varepsilon \geq \varepsilon_d; \end{cases}\tag{5}$$

where K is a proportionality constant. While N is proportional to the number of potential sites for hot spot formation, the rest of the terms can be regarded as the fraction of potential sites that actually become hot spots which depends on η and the level of deformation. In addition to the calculated

TABLE II. Values of the parameters used in Eq. (5).

Parameter			Value
K			1
α_0			1.8
β			1
	Level of lateral confinement		
	Traction –free boundary	$v_L/v = 0.5$	Fully confined $(v_L/v = 0)$
Stress ratio $(\sigma_{xx}/\sigma_{yy})$	0.2	0.3	0.76
α	2.0	2.1	2.56

results, Figs. 12(b) and 12(c) also show fits using Eq. (5) for volume fractions between $\eta = 0.69$–0.82 and different levels of confinement. Clearly, α depends on the degree of confinement, and hence, the stress triaxiality in the specimen. In other words, α is a function of the ratio between the stresses in the lateral and the longitudinal directions. Here, α is assumed to be a linear function of the stress ratio as

$$\alpha = \alpha_0 + \beta \frac{\sigma_{xx}}{\sigma_{yy}}, \qquad (6)$$

where α_0 and β are constants, y represents the loading direction and x is the direction perpendicular to y. σ_{xx} and σ_{yy} are the stresses in the x and y directions averaged over the entire specimen. The values of the constants providing the best fit to the calculated data are shown in Table II.

The value of α increases monotonically with the level of lateral confinement. Also, the higher the value of α, the higher the hot spot density at the same level of overall strain. This trend can be further analyzed by comparing the rates of hot spot formation. The rates are not constant as the deformation progresses. Here, the average rate for strains up to 0.073 is used for comparison. Figure 12(d) shows the average rate for different values of η and levels confinement. The rate for the unconfined case increases proportionally from 10^4 to 4×10^3 per unit cm^2 per unit strain as the volume fraction of the granules increases from 0.69 to 0.82. For the confined case, the corresponding variation is similar,

increasing from 2.4×10^3 to 5×10^3 per unit cm^2 per unit strain. For all packing densities, there is a similar increase of $\sim$1–1.4 $\times 10^3$ per unit cm^2 per unit strain in the rate as the stress state is changes from uniaxial stress to uniaxial strain.

In the case with $\eta = 0.69$, $\dot{\varepsilon} = 16.6 \times 10^3$ s^{-1} [see Fig. 12(a)], beyond $\varepsilon = 0.08$ the number of hot spots is lower than what is predicted by Eq. (5) and is not monotonous. This observation can be explained by considering the unconfined lateral boundary conditions under which fractured surfaces move away from each other, thus decreasing the probability for grain–grain interactions.

It is noted that although the locations of hot spots are random, the total number of hot spots obtained at the macro level are consistent among microstructures with similar attributes under the same loading conditions, as seen in Sec. III B. Also, for most of the calculations, hot spot data and the corresponding fits are obtained up to a nominal strain of 0.1. Additional failure mechanisms may become active at higher strains, affecting hot spot formation beyond the range analyzed here.

E. Hot spot temperatures

The histories of energy dissipations provide insight into the relative importance of the failure mechanisms. We first analyze the effect of strain rate. Figure 13(a) shows the viscoelastic dissipation (W_{ve}) and frictional dissipation (W_f) for a microstructure with $\eta = 0.69$ at the strain rates of 16.6×10^3 s^{-1} and 10^5 s^{-1}. It can be seen that W_{ve} is higher than W_f for all the calculations presented here. However, W_{ve} is a result of deformation of the binder and is dissipated throughout the microstructure, while W_f is distributed mainly along the fractured surfaces in contact. Consequently, hot spot formation is primarily due to frictional dissipation. At the higher rate, higher stresses carried by the binder results in higher W_{ve}. Also, fracture in the grains is more extensive and frictional dissipation (W_f) is higher at the higher rate. The differences in dissipation significantly affect the average temperatures in the hot spots. Figure 14(a) shows the number of hot spots per unit area having different average temperatures at an overall strain of 0.1 for different strain rates between $\dot{\varepsilon} = 16.6 \times 10^3$ and 10^5 s^{-1}.
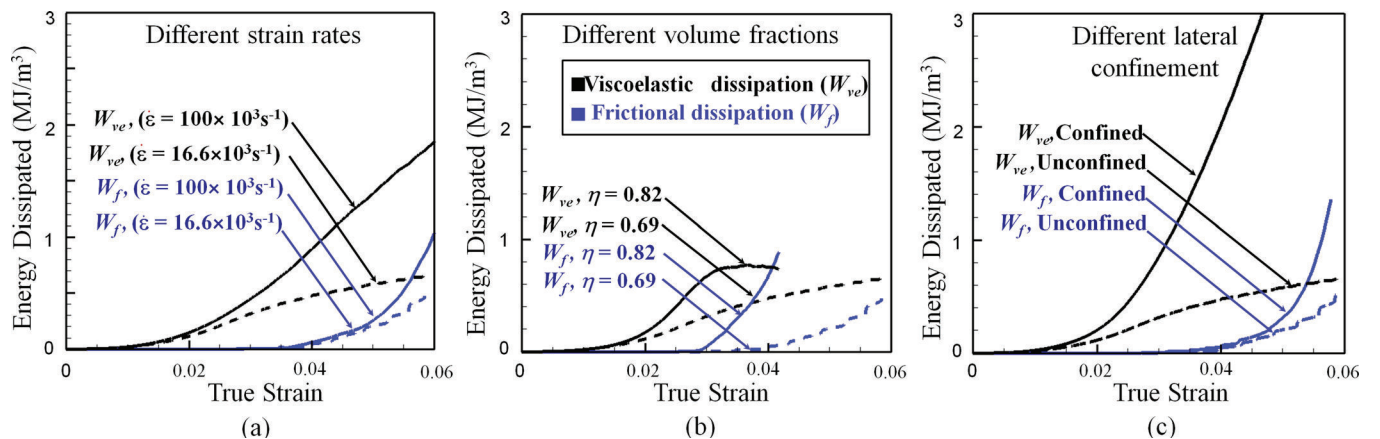

FIG. 13. (Color online) Evolution of dissipation with strain for different (a) strain rates ($\eta = 0.69$, unconfined), (b) volume fractions ($\dot{\varepsilon} = 16.6 \times 10^3$ s^{-1}, unconfined), and (c) levels of lateral confinements ($\dot{\varepsilon} = 16.6 \times 10^3$ s^{-1}, $\eta = 0.69$).
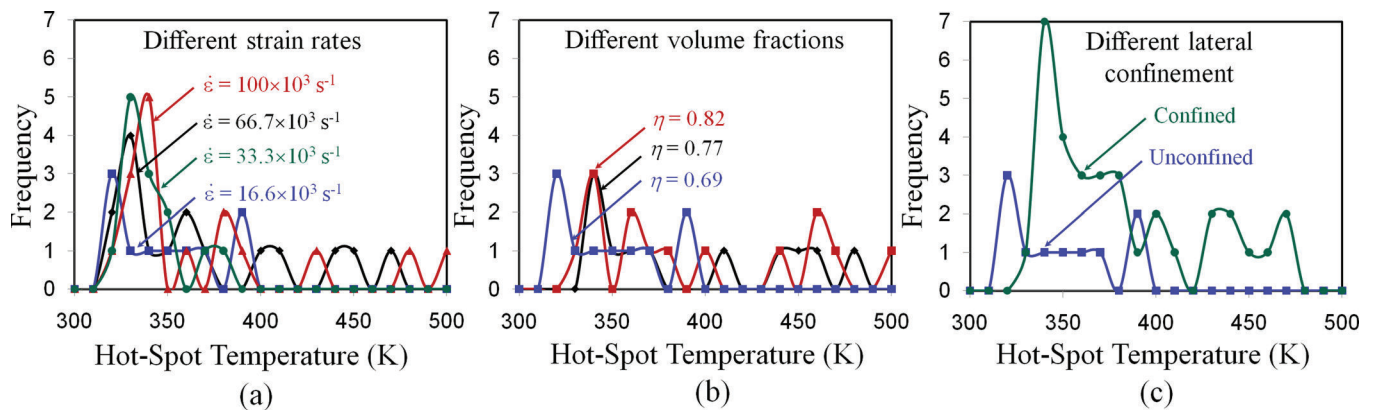
FIG. 14. (Color online) Hot spot temperatures at $\varepsilon = 10\%$ for different (a) strain rates ($\eta = 0.69$, unconfined), (b) volume fractions ($\dot{\varepsilon} = 16.6 \times 10^3$ s^{-1}, unconfined), and (c) levels of lateral confinement ($\dot{\varepsilon} = 16.6 \times 10^3$ s^{-1}, $\eta = 0.69$).

For all cases, the number of hot spots is highest around a certain temperature (T_H). The number of hot spots having temperatures at the high end of the spectrum oscillates and is stochastic. At higher strain rates, the number of hot spots at T_H is higher owing to an increase in the amount of frictional dissipation. T_H increases approximately linearly with strain rate, with the rate of increase being approximately 1.2 K per 10^4 s^{-1} of strain rate increase ($dT_H/d\dot{\varepsilon}$). The results show that higher loading rates lead to higher temperatures in the hot spots, but does not significantly affect the total number of hot spots. It appears that while loading rates affect the temperatures inside hot spots, microstructure (volume fraction, grain size, grain shape, and constituent properties) affects the number of hot spots, with the packing density having, perhaps, the largest influence [Fig. 12(b)].

As the volume fraction of the grains increase, the average thickness of binder between the adjacent grains decreases. As a result, higher stresses develop, leading to earlier fracture and higher frictional dissipation. Figure 13(b) show the histories of energy dissipation for two cases with $\eta = 0.69$ and 0.82 at $\dot{\varepsilon} = 16.6 \times 10^3$ s^{-1}. Both W_{ve} and W_f increase with the volume fraction. However, the increase of W_f is larger than the corresponding increase in W_{ve}. Specifically, at $\varepsilon = 3.5\%$ the increase in W_f is 500% and the increase in compared W_{ve} is 60%. This is primarily due to the earlier and more extensive fracture and frictional dissipation in case of higher volume fraction. Consequently, at the same amount of overall strain, a higher number of hot spots develops as a result of the enhanced frictional dissipation. This is reflected in Fig. 14(b), which shows the distribution of hot spots shifting in the higher temperature direction as η increases from 0.69 to 0.82.

The relative influences of different dissipation mechanisms are also affected by the degree of confinement. Figure 13(c) shows the viscoelastic dissipation in the binder and frictional dissipation at fractured surfaces for two cases, one with confined and other unconfined lateral surfaces, at an overall strain of 0.1 ($\eta = 0.69$, $\dot{\varepsilon} = 16.6 \times 10^3$ s^{-1}). For the confined case, the stress in the binder is much higher and results in higher viscoelastic dissipation. Specifically, the viscoelastic dissipation in the binder at $\varepsilon = 4.0\%$ is 2.4 MJ/m^3 for the confined case and 0.5 MJ/m^3 for the unconfined case. Up to

$\varepsilon = 4.0\%$, frictional dissipation between the two cases of confinement are similar. Beyond this strain, the higher stress levels in the confined specimen lead to a higher amount of fracture and a higher level of subsequent frictional dissipation. Specifically, at $\varepsilon = 5.74\%$, frictional dissipation for the confined case is 1.4 MJ/m^3 while it is 0.5 MJ/m^3 for the unconfined case. The number of hot spots having different average temperatures at an overall strain of 10% is shown in Fig. 14(c) for the two cases. The higher level of frictional dissipation under higher confinement causes the value of T_H (350 K) to be higher than that for the unconfined case (320 K). For the confined specimen, a significant number of hot spots also occur in the temperature range of 400–600 K. On the other hand, for the unconfined specimen, all hot spots have temperatures less than 400 K.

It is worth pointing out that most hot spots occur in the binder or at the binder-granule interfaces. Temperature rises inside the grains are relatively low. The calculated temperatures in a small number of hot spots may reach or exceed the melting temperature of Estane ($\sim$378 K) and approach the melting temperature of β-HMX ($\sim$522 K). Numerically, the situation is handled by formulating the constitutive equations such that as the temperature approaches the melting temperature of the material, the material gradually loses the ability to carry shear stress, but remains able to sustain hydrostatic pressure.

IV. CONCLUSIONS

A fully coupled thermomechanical cohesive finite element framework is used to analyze the response of polymer bonded explosives. The analysis focuses on energy localization at different strain rates for microstructures with different volume fractions of grains under different confinement conditions.

A method for identifying hot spots is developed, allowing the size and temperature distributions of hot spots to be analyzed. Heating due to the viscoelastic deformation of the polymer binder and friction along crack surfaces are the primary mechanisms responsible for the formation of the hot spots. In early stages of the deformation, viscoelastic dissipation is the primary heating mechanisms. In later stages of deformation, the formation of cracks and crack surface contact under compressive stresses lead to more significant heating.

The distribution of hot spots is significantly affected by the strain-rate sensitivity of the binder. At higher loading rates, harder binder response causes hot spots to be localized near the impact face. At lower loading rates, hot spots tend to be more spread out and associated with regions of intense shear deformation of the binder. The average temperature of the hot spots increases with strain rate. The temperature at which the maximum number of hot spots occurs (T_H) increases with loading rate at a rate of approximately 1.2 K per 10^4 s^{-1} of strain rate increase under the conditions analyzed. On the other hand, the total number of hot spots appears insensitive to strain rate (density $\sim$100 cm^{-2}, for $\eta = 0.69$ at $\varepsilon = 0.08$ with unconfined lateral sides) over the range of conditions analyzed.

The strain at which the transition of the dominant heating mechanism from viscoelasticity to friction occurs is primarily dependent on the packing density of the composite as grain–grain interactions play an important role. As a result, the number of hot spots formed increases with packing density η, with the rate of formation being proportional to η.

The analysis shows that stress triaxiality has a significant influence on the density and spatial distribution of hot spots. The hot spots are more densely populated (density $\sim$366 cm^{-2}, for $\eta = 0.69$ at $\varepsilon = 0.08$, confined), are more uniformly distributed spatially and have higher temperatures when the specimen is confined.

Finally, an empirical relation is proposed to quantify the effects of microstructural attributes (volume fraction, grain size, and shape) and loading conditions (degree of confinement) on the evolution of hot spots. This relation provides useful statistical information regarding hot spots and can be used as input, for instance, in continuum level reactive burn models.

ACKNOWLEDGMENTS

[1] S. J. P. Palmer and J. E. Field, Proc. R. Soc. London, Ser. A **383**, 399 (1982).

[2] G. T. Gray, W. R. Blumenthal, D. J. Idar, and C. M. Cady, "Influence of temperature on the high-strain-rate mechanical behavior of PBX 9501," in *Shock Compression of Condensed Matter – 1997*, edited by S. C. Schmidt, D. P. Dandekar, and J. W. Forbes (American Institute of Physics, Melville, NY, 1998), Vol. 429, pp. 583–586.

[3] C. M. Cady, W. R. Blumenthal, G. T. Gray, and D. J. Idar, Polym. Eng. Sci. **46**, 812 (2006).

[4] P. J. Rae, S. J. P. Palmer, H. T. Goldrein, J. E. Field, and A. L. Lewis Proc. R. Soc. London Ser. A **458**, 2227 (2002).

[5] M. R. Baer, Thermochim. Acta **384**, 351 (2002).

[6] R. W. Armstrong and W. L. Elban, Mater. Sci. Eng. A **122**, L1 (1989).

[7] S. G. Bardenhagen, M. G. Stout, and G. T. Gray, Mech. Mater. **25**, 235 (1997).

[8] W. M. Trott, M. R. Baer, J. N. Castaneda, L. C. Chhabildas, and J. R. Asay, J. Appl. Phys. **101**, 21 (2007).

[9] R. Menikoff, "Pore collapse and hot spots in HMX," in *Shock Compression of Condensed Matter -2003, Pts 1 and 2, Proceedings*, edited by M. D. Furnish, Y. M. Gupta, and J. W. Forbes (American Institute of Physics, Melville, NY, 2004), Vol. 706, pp. 393–396.

[10] C. R. Siviour, P. R. Laity, W. G. Proud, J. E. Field, D. Porter, P. D. Church, P. Gould, and W. Huntingdon-Thresher, Proc. R. Soc., Ser. A **464**, 1229 (2008).

[11] P. A. Urtiew and C. M. Tarver, Combust. Explos. **41**, 766 (2005).

[12] H. L. Berghout, S. F. Son, C. B. Skidmore, D. J. Idar, and B. W. Asay, Thermochim. Acta **384**, 261 (2002).

[13] D. J. Idar, R. A. Lucht, J. W. Straight, R. J. Scammon, R. V. Browning, J. Middleditch, J. K. Dienes, C. B. Skidmore, and G. A. Buntain, "Low amplitude insult project: PBX 9501 high explosive violent reaction experiments," in *Proceedings of the 11th Detonation Symposium*, edited by J. M. Short and J. E. Kennedy (Office of Naval Research, Arlington, VA, 1998), pp. 101–110.

[14] C. M. Tarver, S. K. Chidester, and A. L. Nichols, J. Phys. Chem. **100**, 5794 (1996).

[15] Y. Hamate and Y. Horie, Shock Waves **16**, 125 (2006).

[16] P. D. Peterson, J. T. Mang, M. A. Fletcher, B. W. Olinger, and E. L. Roemer, "Influence of pressing parameters on the microstructure, of PBX 9501," in *Shock Compression of Condensed Matter -2003, Parts 1 and 2, Proceedings*, edited by M. D. Furnish, Y. M. Gupta, and J. W. Forbes (American Institute of Physics, Melville, NY, 2004), vol. 706, pp. 796–799.

[17] A. Barua and M. Zhou, Modell. Simul. Mater. Sci. Eng. **19**, 24 (2011).

[18] Y.-Q. Wu and F.-L. Huang, Mech. Mater. **41**, 27 (2009).

[19] J. Zhai, V. Tomar, and M. Zhou, J. Eng. Mater. Technol. Trans. ASME, **126**, 179 (2004).

[20] E. M. Mas and B. E. Clements, "A viscoelastic model for PBX binders," http://lib-www.lanl.gov/la-pubs/00818442.pdf (1996).

[21] A. Barua and M. Zhou, "Heating in microstructures of HMX/Estane PBX during dynamic deformation," Shock Compression of Condensed Matter **56**(6), (2011). http://meetings.aps.org/link/BAPS.2011.SHOCK.Y3.6.

[22] R. K. Govier, G. T. Gray, and W. R. Blumenthal, Metall. Mater. Trans. A **39A**(3), 535 (2008).

[23] N. K. Bourne and G. T. Gray, J. Appl. Phys. **98**, 123503 (2005).

[24] J. Corley, W. Riedel, S. Hiermaier, P. Weidemaier, and M. Thoma, "A combined experimental/computational approach for assessing the high strain rate response of high explosive simulants and other viscoelastic particulate composite materials," in *Shock Compression of Condensed Matter-2001, Parts 1 and 2, Proceedings*, edited by M. D. Furnish (American Institute Physics, Melville, NY, 2002), vol. 620, pp. 705–708.

[25] D. A. Wiegand and B. Reddingius, J. Energ. Mater. **23**, 75 (2005).

[26] C. S. Smith and L. Guttman, Trans. AIME **97**, 81 (1953).